Earth and Planetary Science Letters 541 (2020) 116294

Contents lists available at ScienceDirect

Earth and Planetary Science Letters

www.elsevier.com/locate/epsl

Assessing the potential capability of reconstructing glacial Atlantic water masses and AMOC using multiple proxies in CESM

Sifan Gu [a,b,*], Zhengyu Liu [c,*], Delia W. Oppo [d], Jean Lynch-Stieglitz [e], Alexandra Jahn [f], Jiaxu Zhang [g], Lixin Wu [a,h]

[a] *Physical Oceanography Laboratory, Ocean University of China, Qingdao, China*
[b] *Open Studio for Ocean-Climate-Isotope Modeling, Pilot National Laboratory for Marine Science and Technology (Qingdao), Qingdao, China*
[c] *Atmospheric Science Program, Department of Geography, The Ohio State University, Columbus, OH, USA*
[d] *Department of Geology and Geophysics, Woods Hole Oceanographic Institution, Woods Hole, MA, USA*
[e] *School of Earth and Atmospheric Sciences, Georgia Institute of Technology, Atlanta, GA, USA*
[f] *Department for Atmospheric and Oceanic Sciences and Institute of Arctic and Alpine Research, University of Colorado Boulder, Boulder, CO, USA*
[g] *Computational Physics and Methods (CCS-2) and Center for Nonlinear Studies (CNLS), Los Alamos National Laboratory, Los Alamos, NM, USA*
[h] *Pilot National Laboratory for Marine Science and Technology (Qingdao), Qingdao, China*

ARTICLE INFO

Article history:
Received 2 July 2019
Received in revised form 3 April 2020
Accepted 19 April 2020
Available online 6 May 2020
Editor: L. Robinson

Keywords:
Last Glacial Maximum
AMOC
water mass
multi-proxy

ABSTRACT

Reconstructing the Atlantic Meridional Overturning Circulation (AMOC) during the Last Glacial Maximum (LGM) is essential for understanding glacial-interglacial climate change and the carbon cycle. However, despite many previous studies, uncertainties remain regarding the glacial water mass distributions in the Atlantic and the AMOC intensity. Here we use an isotope enabled ocean model with multiple geotracers ($\delta^{13}C$, ε_{Nd}, ^{231}Pa/^{230}Th, $\delta^{18}O$ and Δ^{14}C) and idealized water tracers to study the potential constraints on LGM ocean circulation from multiple proxies. Our model suggests that the glacial Atlantic water mass distribution can be accurately constrained by the air-sea gas exchange signature of water masses ($\delta^{13}C_{AS}$), but ε_{Nd} might overestimate the North Atlantic Deep Water (NADW) percentage in the deep Atlantic probably because of the boundary source of Nd. A sensitivity experiment with an AMOC of similar geometry but much weaker strength suggests that the correct AMOC geometry is more important than the AMOC strength for simulating the observed glacial $\delta^{13}C$ and ε_{Nd} distributions. The kinematic tracer ^{231}Pa/^{230}Th is sensitive to AMOC intensity, but the interpretation might be complicated by the AMOC geometry and AABW transport changes during the LGM. $\delta^{18}O$ in the benthic foraminifera ($\delta^{18}O_c$) from the Florida Straits provides a consistent measure of the upper ocean boundary current in the model, which potentially provides an unambiguous method to reconstruct glacial AMOC intensity. Finally, we propose that the moderate difference between AMOC intensity at LGM and PD, if any, is caused by the competition of the responses to CO$_2$ forcing and continental ice sheet forcing.

1. Introduction

The Atlantic Meridional Overturning Circulation (AMOC) is an important component in the climate system through its role in redistributing heat, carbon, and nutrients. The upper cell of AMOC is associated with northward-flowing Antarctic Intermediate Water (AAIW) and southward-flowing North Atlantic Deep Water (NADW), and the lower cell of AMOC is associated with Antarctic Bottom Water (AABW). Boundary conditions during the Last Glacial Maximum (LGM; ∼23-18ka) differ significantly from the present day (PD), dominated by a ∼100 ppm lower atmospheric CO$_2$, greatly expanded continental ice sheets and sea ice. Accurate reconstructions of the AMOC strength and geometry, as well as deepwater properties during the LGM, are needed for understanding the glacial-interglacial climate change and the carbon cycle.

Although a shallower glacial AMOC upper cell than PD has been inferred from proxies such as $\delta^{13}C$, Cd/Ca and ε_{Nd} (e.g., Curry and Oppo, 2005; Howe et al., 2016; Marchitto and Broecker, 2006) and is considered a robust feature, there are uncertainties in the extent of the LGM Atlantic water masses. It is still heavily debated whether the water in the LGM deep Atlantic was northern-sourced, southern-sourced, or a mixture of both sources. Nutrient-related proxies such as $\delta^{13}C$ and Cd/Ca suggest the dominance of the

---

* Corresponding authors at: Physical Oceanography Laboratory, Ocean University of China, Qingdao, China and Atmospheric Science Program, Department of Geography, The Ohio State University, Columbus, OH, USA.
E-mail addresses: gusifan@gmail.com (S. Gu), liu.7022@osu.edu (Z. Liu).

https://doi.org/10.1016/j.epsl.2020.116294
0012-821X/

glacial AABW over NADW in the deep Atlantic (e.g., Curry and Oppo, 2005; Marchitto and Broecker, 2006). However, a water mass decomposition using an inversion of $\delta^{13}C$ and $\delta^{18}O$ data suggests that although AABW fraction increased in the deep Atlantic during LGM, the AABW was not as spatially extensive as suggested previously (Gebbie, 2014). A more recent inversion using $\delta^{13}C$, $\delta^{18}O$ and Cd/Ca (Oppo et al., 2018) suggests that the replacement of NADW by AABW leads to the $\delta^{13}C$ and Cd/Ca changes in the deep Atlantic. Taking ε_{Nd} reconstructions in the Atlantic at face values suggests that the deep glacial Atlantic contained a significant fraction of NADW instead of being overwhelmed by AABW (Howe et al., 2016).

Similarly, previous studies have used proxy records, numerical models, or their combination, to reconstruct the vigor of AMOC during the LGM. However, it is still highly uncertain if the AMOC strength was stronger or weaker at LGM than the present day. Circulation rate estimated from geotracers such as sediment ^{231}Pa/^{230}Th provides a range of estimates regarding glacial AMOC strength. Earlier ^{231}Pa/^{230}Th reconstructions suggest weaker (Böhm et al., 2014; McManus et al., 2004), or indistinguishable (Yu et al., 1996) glacial AMOC from the PD, while a more recent ^{231}Pa/^{230}Th compilation suggests a stronger LGM southward transport in the eastern Atlantic but a weaker LGM transport in western Atlantic (Ng et al., 2018). Combining ^{231}Pa/^{230}Th reconstructions and a 2-D scavenging model suggests that the LGM AMOC was at least as strong as the PD AMOC (Lippold et al., 2012). Density reconstructions from $\delta^{18}O$ of benthic foraminifera ($\delta^{18}O_C$) in the Florida Straits suggest a weaker LGM AMOC (Lynch-Stieglitz et al., 1999). PMIP atmosphere-ocean general circulation models under glacial boundary conditions show no agreement on either the geometry or the strength of the LGM AMOC (Muglia and Schmittner, 2015; Otto-Bliesner et al., 2007; Weber et al., 2007), which has been attributed to different Antarctic sea-ice formation (Marzocchi and Jansen, 2017), initial conditions, and insufficient equilibrium (Zhang et al., 2013). Recent studies combining numerical models and proxy reconstructions suggest either a stronger AMOC (data assimilation method using δ^{18}O and δ^{13}C records; Kurahashi-Nakamura et al., 2017) or a weaker AMOC (fitting simulated carbon isotopes to LGM reconstructions; Hesse et al., 2011; Menviel et al., 2017; Muglia et al., 2018).

Here, we provide further insights into the glacial AMOC and the water mass distributions in the Atlantic by evaluating the ability of different tracers to constrain the glacial water mass distributions and the glacial AMOC intensity. For this purpose, we use simulations of oceanic $\delta^{13}C$, ε_{Nd}, ^{231}Pa/^{230}Th, radiocarbon, and $\delta^{18}O$ under LGM boundary conditions with the Community Earth System Model (CESM). One distinct feature of our study from previous ones (e.g. Menviel et al., 2017; Muglia et al., 2018) is that our model simulates multiple geotracers, including $\delta^{13}C$, ^{231}Pa/^{230}Th, ε_{Nd}, radiocarbon, and $\delta^{18}O$, allowing a direct comparison with multiple paleo proxies simultaneously, providing a potentially more comprehensive constraint on glacial circulation and water masses.

2. Methods

2.1. Isotope-enabled ocean model

In this study, we use the Parallel Ocean Program version 2 (POP2) (Danabasoglu et al., 2012) with active biogeochemistry, which is the ocean component of the Community Earth System Model (CESM). It has 60 vertical layers with a nominal 3° horizontal resolution. Several isotope-based proxy systems have now been added to this ocean model, creating an isotope-enabled version of POP (iPOP2): carbon isotopes (^{13}C and ^{14}C) (Jahn et al., 2015), neodymium isotopes (^{143}Nd and ^{144}Nd) (Gu et al., 2019a), ^{231}Pa/^{230}Th (Gu and Liu, 2017), and δ^{18}O (Zhang et al., 2017). Here we use the version of fixed particle flux for ε_{Nd} and ^{231}Pa/^{230}Th and abiotic Δ^{14}C (uncoupled to the biogeochemical model) to simplify the interpretations of these three proxy distributions so that simulated differences between the LGM and PD distributions are associated only with the physical circulation. However, the ^{13}C is coupled to the biogeochemical model. Isotopes (ε_{Nd}, ^{231}Pa/^{230}Th, $\delta^{13}C$ and Δ^{14}C) in iPOP2 have been validated against the PD seawater observations in previous studies (Gu et al., 2019a; Gu and Liu, 2017; Jahn et al., 2015). A brief discussion of quantitative model-data comparisons and the model biases is also included in the Supplementary Materials (SM text 2-4) for reference. Overall, isotope distributions in iPOP2 are validated against modern observations and capture the key signatures in the Atlantic for the purpose of this study.

To quantify the insulation effect of sea ice in regulating the air-sea exchange, therefore, the radiocarbon age, we implemented two idealized water age tracers: the ideal age and the idealized ventilation age (Zhang, 2016). Ideal age is set to 0 at the ocean surface and increases at the rate of 1 yr/yr in the ocean interior. Idealized ventilation age is the same as the ideal age except that it is not set to 0 if the ocean surface is covered by sea ice; instead, its surface value is set depending on the ice fraction (Zhang, 2016), making it always older than the ideal age itself.

Finally, identification of the distribution of subsurface Atlantic water mass mixtures is facilitated by passive dye tracers. The dye tracers are released at surface, which is done by fixing the value at 1 in different surface regions and fixed at 0 outside each region at each time step (Gebbie, 2014): 40°N-80°N in the North Atlantic (Dye-North), 40°S-40°N in the Atlantic (Dye-Subtropical), and south of 40°S in the global ocean (Dye-South).

2.2. Experiments

We analyze the model LGM in a transient ocean simulation from 20ka to Holocene (called C-iTRACE, described in detail in Gu et al., 2019b) using iPOP2 in this study. The 100-years average from 19.1ka to 19.0ka in C-iTRACE is used as the model LGM. In C-iTRACE, iPOP2 was forced by monthly surface forcing from a coupled transient simulation from the LGM to the Holocene (TRACE21) which simulates many features of the deglacial climate (e.g., Liu et al., 2009). The neodymium sources are fixed in C-iTRACE. C-iTRACE can reproduce the ocean circulation in TRACE21 (Gu et al., 2019b) and the advantage of C-iTRACE experiment is that it has multiple geotracers that can be compared directly with proxies measured in sediment cores. The details of the initial condition and spin-up for carbon isotopes, ε_{Nd}, and ^{231}Pa/^{230}Th are described in SM text 1.

The LGM atmospheric boundary conditions for carbon isotopes were set as follows: pCO$_2$ is 188 ppmv, $\delta^{13}CO_2$ is $-6.45‰$, Δ^{14}CO$_2$ is 398‰ in the Northern Hemisphere, 394‰ in the equatorial region, and 390‰ in the Southern Hemisphere. The dust deposition used for the LGM period was from Mahowald et al. (2006).

For the comparison of the circulation and tracer distributions between LGM and PD, we use a PD control experiment forced by CORE-II data (Large and Yeager, 2008). The PD experiment in this study is used as “Holocene” when comparing the model results to the observational difference between LGM and Holocene because the difference between PD and Holocene is much smaller than the difference between the LGM and Holocene and therefore has little impact on our conclusions.

In C-iTRACE, meltwater flux is added to North Atlantic beginning at 19ka. While we focus on the LGM and LGM-Holocene differences, we also use some results from 17.5ka in C-iTRACE as an LGM hosing sensitivity experiment (LGM-hosing) to isolate the effect of AMOC strength changes on the simulated tracer distribu-

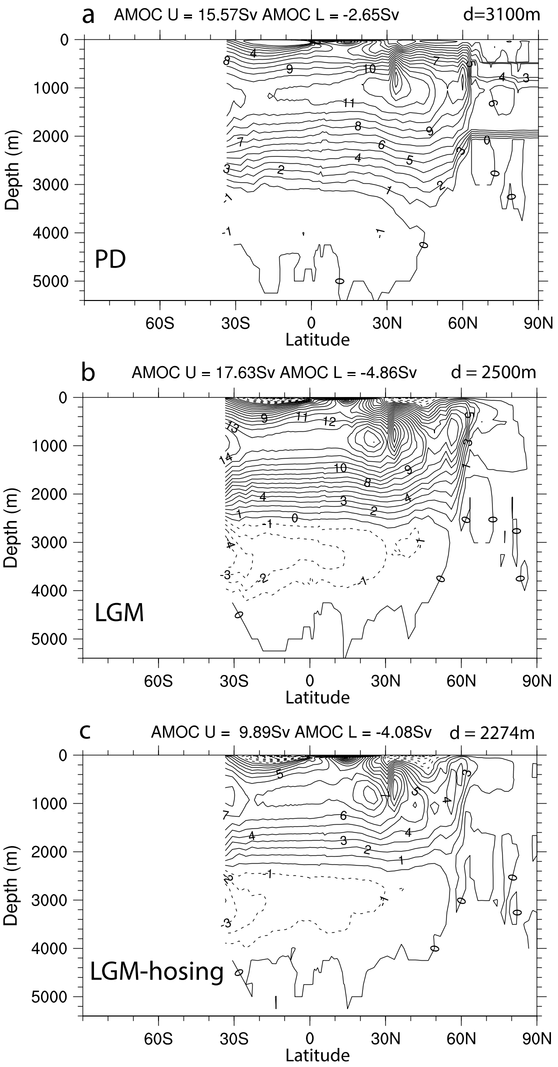

Fig. 1. AMOC during PD (a), LGM (b), and LGM-hosing (c). The AMOC upper cell strength is defined as the maximum zonal mean Atlantic streamfunction below 500 m between 20°N and 60°N. The AMOC lower cell strength is defined as the minimum zonal mean Atlantic streamfunction below 2000 m. The depth of the zero-contour averaged between 45°N to 35°S as used as the AMOC depth.

tions. LGM-hosing has a similar water mass geometry to the LGM but with a weaker AMOC strength. In LGM-hosing, the atmospheric CO_2 level is 189 ppmv, with the $\delta^{13}CO_2$ of $-6.40‰$, $\Delta^{14}CO_2$ of 391‰ in the Northern Hemisphere, 387‰ in the equatorial region, and 384‰ in the Southern Hemisphere. These surface forcings are all similar to the LGM setting.

3. Glacial AMOC geometry and water mass distributions

3.1. Model-data comparison

The simulated LGM AMOC upper cell is 600-m shallower than the PD (Fig. 1). The LGM AMOC upper cell strength (17.6Sv) is comparable with the PD strength (15.6Sv), and the LGM lower cell strength (4.9Sv) is almost twice the PD strength (2.7Sv).

The simulated LGM $\delta^{13}C$ in the Atlantic suggests shallower NADW than the PD. Higher modeled LGM values in the upper North Atlantic and lower LGM values in the deep Atlantic and upper South Atlantic agree with observations (Fig. 2 a-c). Quantitatively, the correlation with the Atlantic LGM $\delta^{13}C$ from Oppo et al. (2018) is 0.76, and the root mean square error (RMSE) is 0.40‰. The model-data agreement of LGM $\delta^{13}C$ is similar to Muglia et al. (2018): the correlation with the global LGM $\delta^{13}C$ observations (Peterson et al., 2014) is 0.8, and the RMSE is 0.36‰, which are comparable to 0.79, and 0.33‰ in Muglia et al. (2018) respectively (Table S1).

Modeled LGM ε_{Nd} also shows shoaled NADW. The unradiogenic ε_{Nd} associated with the NADW penetrates to 40°S at 2500 m during the LGM (Fig. 2e), which is consistent with the ε_{Nd} pattern in Howe et al. (2016). The correlation with the Atlantic ε_{Nd} from Howe et al. (2016) is 0.63, and the RMSE is 1.36. The most significant feature of the ε_{Nd} difference between LGM and PD is an $\sim$2 ε_{Nd} unit of the radiogenic shift below 2500 m. This more radiogenic deep Atlantic during LGM agrees with the observational difference, although the magnitude of change is somewhat larger in the observations ($\sim$3 ε_{Nd} unit) (Fig. 2f). The radiogenic change in the deep Atlantic appears to be caused by the upward shift of the unradiogenic NADW and the increased strength of the AABW cell, which results in stronger northward transport of radiogenic AABW during the LGM.

Our model simulates a higher ventilation age at LGM than PD in the deep Atlantic below 2500 m, mainly because of increased sea ice in the Southern Ocean. The radiocarbon ventilation age (B-A age) is calculated as the benthic-atmosphere age differences: $8267 \times \ln\left(\frac{\frac{\Delta^{14}C_{Atm}}{1000}+1}{\frac{\Delta^{14}C_{Ocean}}{1000}+1}\right)$ (^{14}C half-life is 5730 years). In the glacial Atlantic, the B-A age and the idealized ventilation age below 2500 m are significantly increased during the LGM compared to the PD (Fig. 3c and 3f) as in the proxy records (Freeman et al., 2016). In contrast, the ideal age is reduced in the Southern Ocean and most of the deep Atlantic in the LGM simulation (Fig. 3i) due to the almost twice than PD AMOC lower cell strength and, in turn, the AABW export. Since the only difference between the idealized ventilation age and the ideal age in the model is the insulation effect of sea ice on air-sea exchange, similar to the case of radiocarbon (Zhang, 2016), the increased B-A age/idealized ventilation age in the deep Atlantic at LGM is caused mainly by the expansion of sea ice in the Southern Ocean. In the meantime, the deep North Atlantic around 3000 m in the LGM simulation is no longer ventilated by the AMOC upper cell as in the PD simulation, which leads to the increased idealized ventilation age/B-A age in the deep North Atlantic, with the maximum increase at around 3000 m (Fig. 3c and 3f).

By removing the influence of biological processes on $\delta^{13}C$, the air-sea gas exchange signature of benthic $\delta^{13}C$ ($\delta^{13}C_{AS}$) is nearly conservative and therefore may serve as a tracer of water mass (Broecker and Maier-Reimer, 1992; Lynch-Stieglitz and Fairbanks, 1994). Following Broecker and Maier-Reimer (1992), $\delta^{13}C_{AS}$ can be estimated approximately from $\delta^{13}C$ and PO_4 (SM text 6). The $\delta^{13}C_{AS}$ during the PD reflects the major water mass distributions in the Atlantic and $\delta^{13}C_{AS}$ from the Southern Ocean is higher than the North Atlantic (Fig. 5a), which is consistent with the $\delta^{13}C_{AS}$ estimated from modern observations (Gebbie, 2014). However, model LGM $\delta^{13}C_{AS}$ in the Southern Ocean remains higher than the North Atlantic, which is opposite to the LGM foraminifera-based $\delta^{13}C_{AS}$ estimates that suggest LGM values were higher in the glacial North Atlantic than the Southern Ocean, and overall very low $\delta^{13}C_{AS}$ in the Southern Ocean (Oppo et al., 2018). The model-data discrepancy is related to the $\sim$1‰ higher model $\delta^{13}C$ than observations in the Southern Ocean. Regardless of this potential model bias, $\delta^{13}C_{AS}$ in the LGM simulation still traces different water masses from their surface origins in the model, such as the low $\delta^{13}C_{AS}$ originated from the North Atlantic in the mid-depth Atlantic around 2000 m (Fig. 5d). In addition, the $\delta^{13}C_{AS}$ difference between LGM and PD in the model (Figure S7) agrees with the observational estimation in Oppo et al. (2018) for the increase in the North Atlantic and decrease in the Southern Ocean, albeit with a

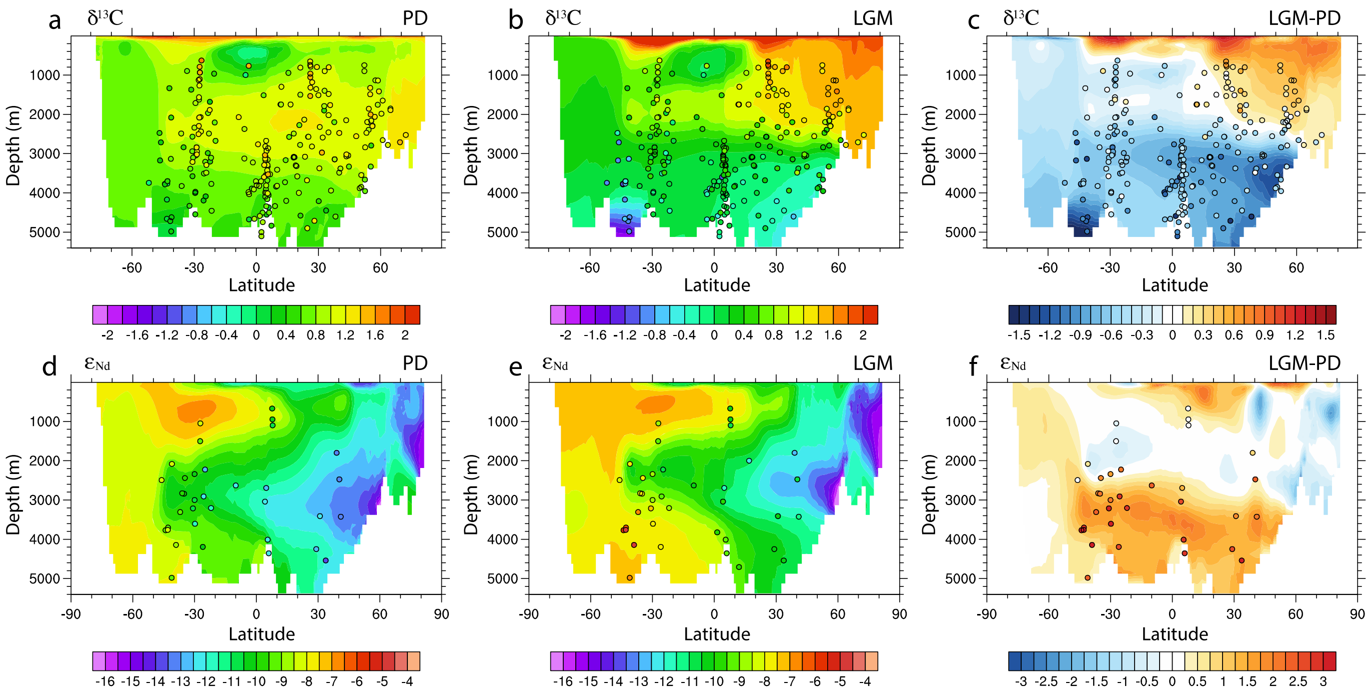

Fig. 2. Modelled Atlantic tracer distributions during PD, LGM, and the differences between the LGM and the PD. (a-c) Atlantic zonal mean $\delta^{13}C$. (d-f) Atlantic zonal mean ε_{Nd}. Observations are overlaid using the same colormap in (a)-(f). The $\delta^{13}C$ observations are from Peterson et al. (2014). The ε_{Nd} observations are from Howe et al. (2016). The observations overlaid on modelled PD tracer distributions are observations for the Holocene and the observations overlaid on modelled difference between LGM and PD are observational differences between LGM and Holocene. (For interpretation of the colors in the figure(s), the reader is referred to the web version of this article.)

smaller magnitude in the model that is related to the model-data discrepancy discussed above.

Overall, the simulated difference between LGM and PD of Atlantic zonal mean matches the major features suggested in the observations. For these major differences, the eastern Atlantic and western Atlantic show a similar difference between LGM and PD (Figure S6).

3.2. *Tracking LGM water mass distributions in the Atlantic*

In observational studies, Atlantic water mass distributions have been inferred from $\delta^{13}C_{AS}$ (e.g., Lynch-Stieglitz and Fairbanks, 1994) and ε_{Nd} (Howe et al., 2016). In a model such as CESM, the Atlantic water mass distributions can be identified unambiguously using dye tracers. Here, the $\delta^{13}C_{AS}$ and ε_{Nd} are compared with the idealized dye tracers to test the ability of $\delta^{13}C_{AS}$ and ε_{Nd} to reconstruct water mass distribution in the Atlantic.

The idealized dye concentrations indicate that the Atlantic water mass distributions are significantly different between the LGM and the PD simulations, with NADW replaced by the AABW in the deep Atlantic at LGM (Fig. 4). The core of NADW ascends from ∼2500 m in the PD (Fig. 4b) to ∼2000 m in the LGM (Fig. 4a); The span of the 50% contour of the Dye-North is reduced from between 1000 m and 4000 m at PD to between 1000 m and 3000 m at the LGM in the Atlantic, with the AABW occupying a larger volume in the deep Atlantic at LGM (Fig. 4f); The boundary between the NADW and the AABW shoals from 3000 m at PD to 2500 m at LGM. The largest change of water mass is in the North Atlantic near 3500 m (Fig. 4c and 4f), where the water mass dominated by NADW at PD is replaced by AABW at LGM. The AAIW is shallower during the LGM than the PD, consistent with the model-data comparison study of Gu et al. (2017). During the LGM, the subtropical water sinks to a deeper depth than the PD in the Northern Hemisphere (Fig. 4g-i). The water mass changes suggested by the dye tracers between the LGM and the PD agrees with the modeling results in Oppo et al. (2018) for the decrease of NADW and increase of AABW in the deep Atlantic and the increased subtropical water at the intermediate depth in the North Atlantic during the LGM. However, the largest change is located in the bottom of the North Atlantic in Oppo et al. (2018), instead of near 3500 m as in this study.

The $\delta^{13}C_{AS}$ can be used to calculate the NADW and AABW percentage using binary mixing by assuming $\delta^{13}C_{AS}$ end-member values (SM text 7). The NADW% and AABW% calculated from $\delta^{13}C_{AS}$ matches the dye concentrations excellently (Fig. 5). The NADW% by $\delta^{13}C_{AS}$ is highly correlated with Dye-North in both PD and LGM ($r_{PD} = 0.93$ and $r_{LGM} = 0.97$) and the AABW% by $\delta^{13}C_{AS}$ is also highly correlated with Dye-South at both PD and LGM ($r_{PD} = 0.92$ and $r_{LGM} = 0.97$). Therefore, our model suggests that $\delta^{13}C_{AS}$ is an excellent tracer for NADW and AABW in the Atlantic, as long as the source region can be identified.

In comparison, water mass percentage in the Atlantic inferred from ε_{Nd} (Howe et al., 2016) (SM text 8) shows a water mass percentage different from the idealized dye tracers, with the ε_{Nd} overestimating the NADW% in the deep Atlantic. In Howe et al. (2016), the NADW% below 3000 m is about 70% in the North Atlantic, which was inferred as evidence of the presence of NADW in the deep Atlantic, challenging the notion that the AABW dominated the deep glacial Atlantic. The modeled NADW%, assuming conservative mixing of water masses with different end-member ε_{Nd} values, is also about 70% in the deep Atlantic during the LGM (Fig. 6e), but the Dye-North concentration indicates that the true model NADW% is less than 10% (Fig. 4b). The modeled AABW% estimated by ε_{Nd} suggests less than 50% AABW in the deep North Atlantic during the LGM (Fig. 6f), but the Dye-South suggests a value closer to 90% below 3000 m (Fig. 4e). These comparisons between the water mass percentage reconstructed from ε_{Nd} and the idealized dye tracers shows that ε_{Nd} overestimates NADW% and underestimates AABW% in deep Atlantic, suggesting that the distribution of ε_{Nd} in the deep Atlantic is controlled by more than just mixing of water masses as discussed below.

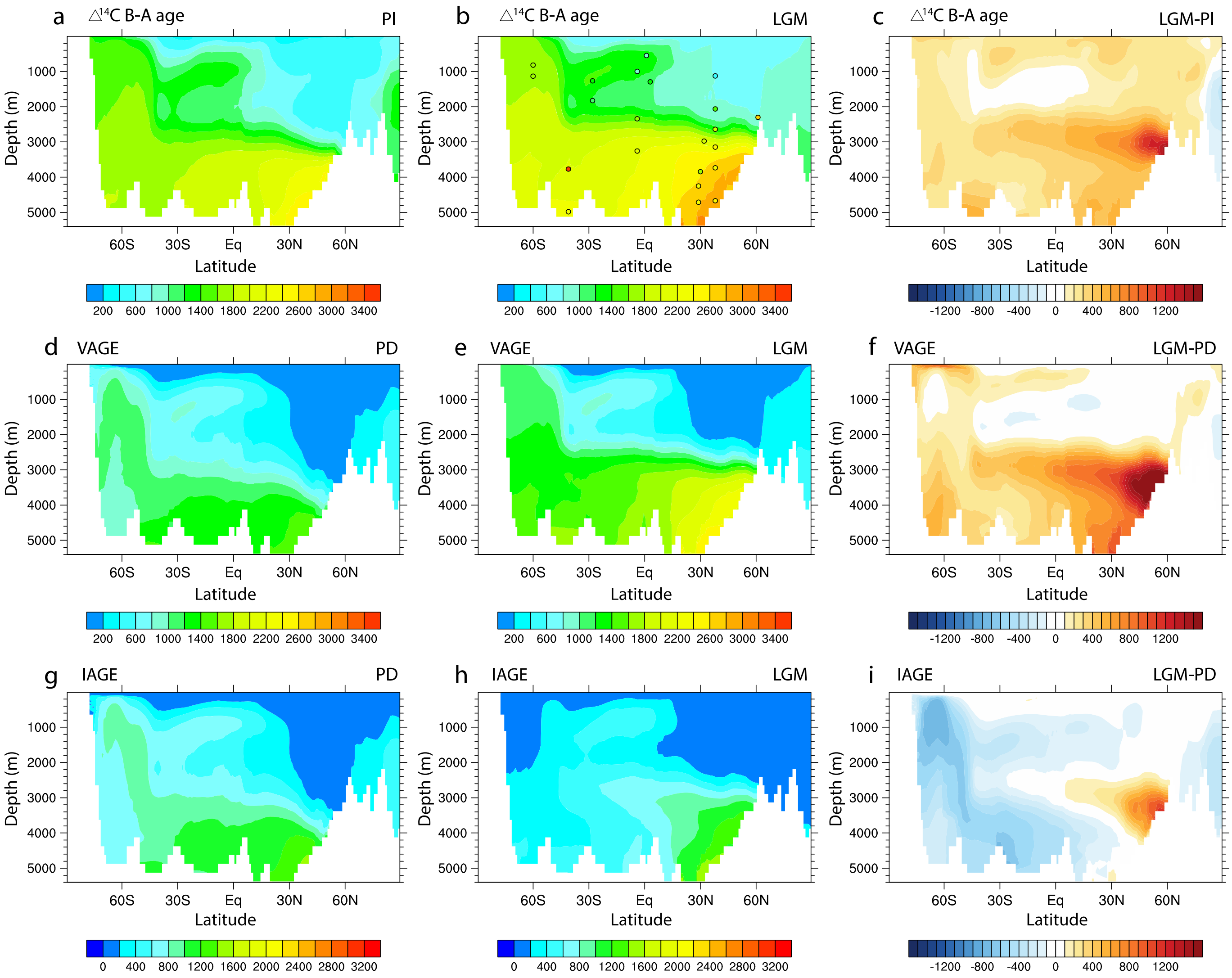

Fig. 3. The Atlantic zonal mean water ages during PD, LGM and the differences between the LGM and the PD: radiocarbon ventilation age (a-c), idealized ventilation age (d-f), and ideal age (g-i). The preindustrial Δ^{14}C instead of the PD Δ^{14}C is used to exclude the influence of the nuclear bomb test. The observational LGM radiocarbon age is from the compilation in Menviel et al. (2017).

The overestimated NADW% in the deep Atlantic suggested by ε_{Nd} is probably caused by the unradiogenic boundary source of Nd near 3000 m in the Labrador Sea (SM text 3 and Figure S1 and S3). The pattern correlation between the NADW% calculated from ε_{Nd} and Dye-North is 0.53 during the PD and 0.48 during the LGM, which is much lower than the correlation between the $\delta^{13}C_{AS}$ and Dye-North (0.93 and 0.97 respectively, Table S4). Unlike the $\delta^{13}C_{AS}$ and the dye tracers, which are both determined entirely by the boundary condition at the surface, ε_{Nd} is controlled by both surface sources and the boundary source at the continental margins, with the boundary source being more important for deep water (Rempfer et al., 2011). Therefore, the unradiogenic ε_{Nd} in the Atlantic comes from both the surface and bottom in the North Atlantic, which are also present in the ε_{Nd} reconstructions in Howe et al. (2016) (their Figure 3). With the additional unradiogenic ε_{Nd} boundary source located near 3000 m in the North Atlantic, the NADW% estimated from ε_{Nd} is deeper than the NADW suggested by Dye-North and $\delta^{13}C_{AS}$.

Furthermore, the overestimated LGM NADW% in the deep North Atlantic is also associated with the unradiogenic ε_{Nd} below 3000 m in the North Atlantic (Fig. 6d and 6e). The modeled ε_{Nd} shows a north-south gradient in the deep Atlantic below 3000-m during the LGM, which agrees with observations (Figure S3), while Dye-North is uniform (Fig. 4b). The ε_{Nd} north-south gradient in the deep Atlantic should be related to the boundary source since if ε_{Nd} were only set by the surface, the distribution of ε_{Nd} should be similar to dye tracers and $\delta^{13}C_{AS}$, both of which are uniform below 3000 m during the LGM. However, the boundary source of ε_{Nd} is only applied above 3000 m. The unradiogenic ε_{Nd} in the deep North Atlantic below 3000 m is therefore caused, additionally, by the reversible scavenging, which transports the unradiogenic ε_{Nd} at 3000 m downward by sinking particles (Gu et al., 2019a; Rempfer et al., 2011), leading to the unradiogenic ε_{Nd} below 3000 m in the North Atlantic. This unradiogenic ε_{Nd} in the deep North Atlantic does not seem to depend critically on model parameters in iPOP2 (Figure S2 and SM text 5). The comparison between ε_{Nd} and dye tracers in the model suggests that the interpretation of ε_{Nd} as water mass composition in deep North Atlantic might be complicated by Nd boundary source and reversible scavenging, which could lead to an overestimation of NADW% in that region. This potential caveat of ε_{Nd} can be further validated by more observations of other water mass proxies with latitudinal coverage in the deep Atlantic in the future, and also by modeling studies in other models.

The comparison of $\delta^{13}C_{AS}$ and ε_{Nd} with the dye tracers in the model suggests that, ideally, $\delta^{13}C_{AS}$ can be used to reconstruct

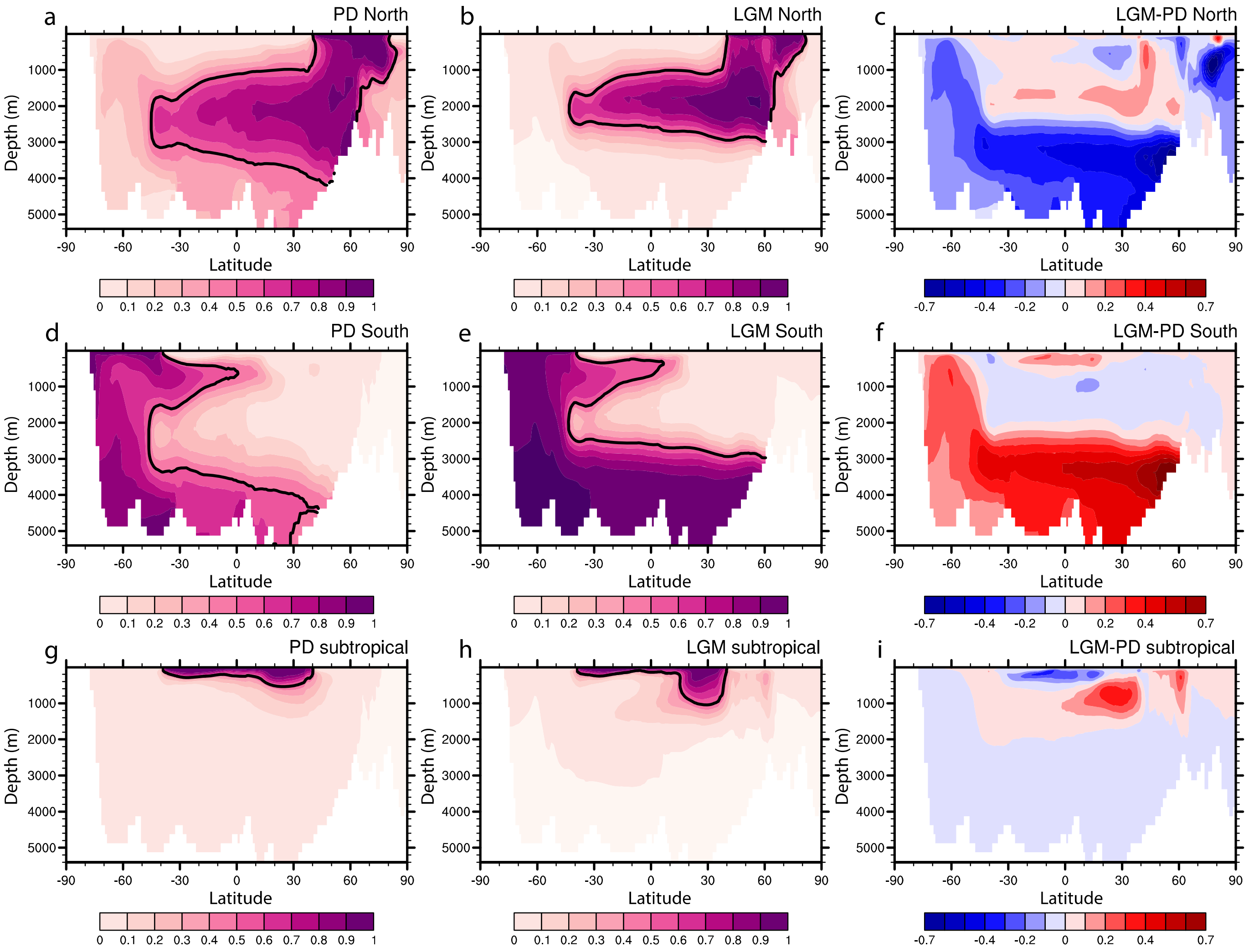

Fig. 4. Percentage of water sourced from different regions in the Atlantic during PD (first column), LGM (second column), and the difference between the LGM and the PD (third column): water originating from the North Atlantic (a-c), water originating from the Southern Ocean (d-f), and water originating from the subtropical region (g-i). The thick black contours on the LGM and the PD water percentage represent the value of 50%.

the water mass distributions more correctly than ε_{Nd}. However, the use of $\delta^{13}C_{AS}$ to reconstruct past water masses in real-world observations might not be as good as in the model due to the uncertainties in retrieving seawater $\delta^{13}C$ and Cd as well as estimating PO_4 from Cd (Middag et al., 2018). Nevertheless, if $\delta^{13}C_{AS}$ can be accurately estimated from paleoceanographic data, it would provide an excellent proxy for reconstructing water masses in the Atlantic.

4. Glacial AMOC strength

4.1. Sensitivity of $\delta^{13}C$ and ε_{Nd} to AMOC strength

Fitting the modeled carbon isotopes under different ocean circulation states to the observational carbon isotopes, two recent studies (Menviel et al., 2017; Muglia et al., 2018) suggested that the LGM carbon isotopes are consistent with a shallower and weaker AMOC at LGM than PD. However, with a shallower but slightly stronger AMOC at LGM, our simulation can also reproduce the major features of different tracer distributions with the agreement quantitatively comparable with the global $\delta^{13}C$ of Muglia et al. (2018).

To further test the tracer distribution sensitivity to AMOC strength, we use LGM-hosing experiment which is characterized by a weak and shallow AMOC state. The major difference between the LGM-hosing and the LGM simulations is the AMOC upper cell strength. In LGM-hosing, the AMOC upper cell strength is 9.9Sv (Fig. 1c), which is about 8Sv (~ 50%) weaker than at LGM. The deep convection regions are similar between LGM and LGM-hosing. The AMOC lower cell strength is 4.1Sv, which is similar to the LGM. The AMOC depth in LGM-hosing is 2274 m, which is only slightly shallower (~250 m) than the LGM.

The $\delta^{13}C$ and ε_{Nd} in LGM-hosing show similar distributions to the LGM. The relatively high $\delta^{13}C$ and unradiogenic ε_{Nd} associated with the NADW originated from the North Atlantic still penetrates to the South Atlantic above 2000 m in LGM-hosing (Fig. 7). Averaged over the Atlantic basin, the $\delta^{13}C$ at the mid-depth around 2000 m in LGM-hosing is generally 0.3‰ lower than the LGM, probably due to the increased remineralization in response to the weaker AMOC upper cell in LGM-hosing (e.g., Schmittner and Lund, 2015); the ε_{Nd} shows a similar unradiogenic minimum at 2500 m in both LGM-hosing and LGM, although the value in LGM-hosing is smaller than at LGM by 0.5 in the upper ocean. More quantitatively, there is no significant difference between the fits of the LGM-hosing $\delta^{13}C$ with the LGM $\delta^{13}C$ data and the model LGM $\delta^{13}C$ with the LGM $\delta^{13}C$ data in the Atlantic and over the globe (Table S1). The model LGM and LGM-hosing states both agree with the global $\delta^{13}C$ data of comparable accuracy with Muglia et al.

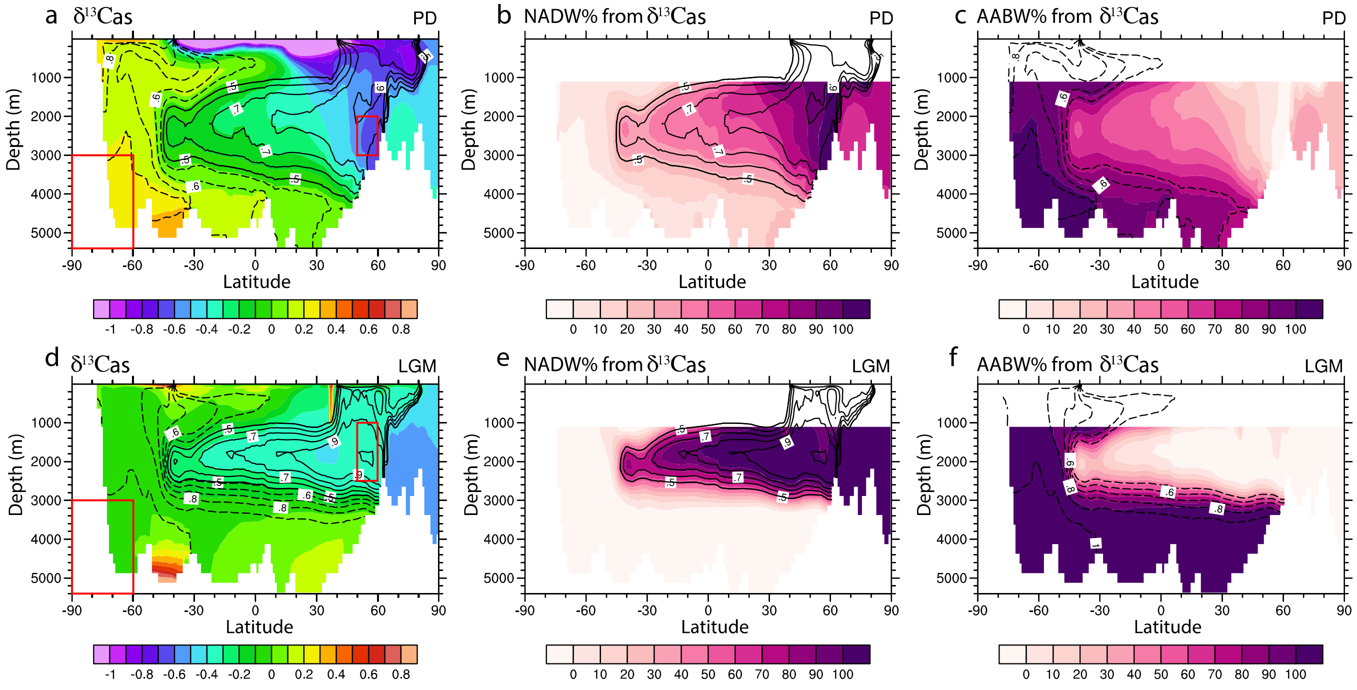

Fig. 5. $\delta^{13}C_{AS}$ and the NADW% and AABW% reconstructed from $\delta^{13}C_{AS}$ during PD (a-c) and LGM (d-e). Dye-North (solid) and Dye-South (dash) contours from 0.5 to 1 are overlaid. Red boxes indicate the regions for calculating NADW and AABW end-members. The water mass percentage is calculated below 1000 m to exclude the AAIW. The NADW end-member is defined as the average of $\delta^{13}C_{AS}$ between 50°N and 60°N from 1000 m to 2500 m during the LGM and from 2000 m to 3000 m during PD in the Atlantic. The AABW end-member is defined as the average of $\delta^{13}C_{AS}$ south of 60°S below 3000 m in the Southern Ocean.

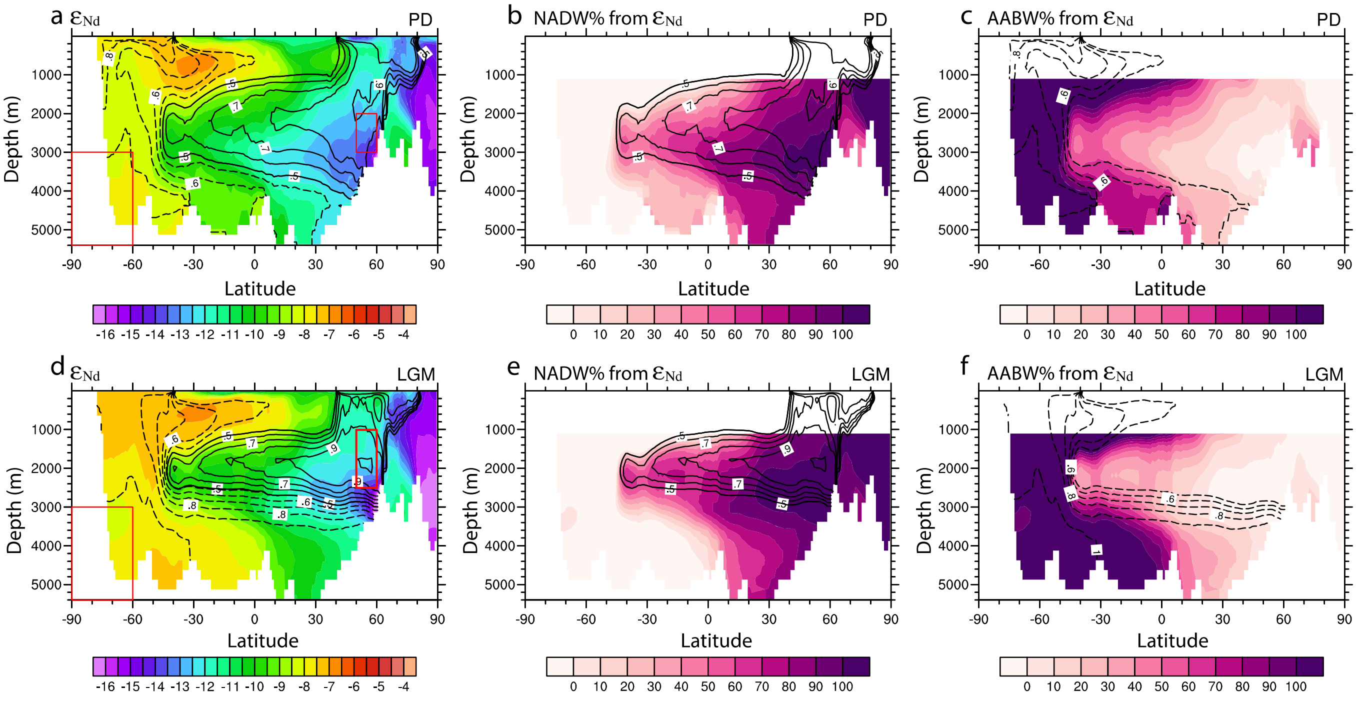

Fig. 6. ε_{Nd} and the NADW% and AABW% reconstructed from ε_{Nd} during PD (a-c) and LGM (d-e). Dye-North (solid) and Dye-South (dash) contours from 0.5 to 1 are overlaid. Red boxes indicate the regions for calculating NADW and AABW end-members, which are defined the same way as in Fig. 6.

(2018) (Table S1). Similar to $\delta^{13}C$, the model-data fit of ε_{Nd} does not show a considerable difference between LGM-hosing and the LGM (Table S1). Therefore, it appears impossible to differentiate between the strong LGM AMOC scenario and the weak LGM-hosing AMOC scenario based on the model-data fit in the two water mass tracers of $\delta^{13}C$ and ε_{Nd} only.

In the model simulations of Menviel et al. (2017) and Muglia et al. (2018), a stronger AMOC strength is always accompanied by a deeper AMOC depth and therefore they do not include an experiment with a strong and shallow AMOC. Therefore, they were unable to test against a strong and shallow AMOC with the glacial carbon isotope distributions. Here, we show that both a strong and shallow AMOC (LGM) and a weak and shallow AMOC (LGM-hosing) can reproduce the glacial $\delta^{13}C$ and ε_{Nd} reconstructions with comparable accuracy. Furthermore, if we use the PD as a case for strong and deep AMOC to compare the modeled $\delta^{13}C$ and ε_{Nd} with

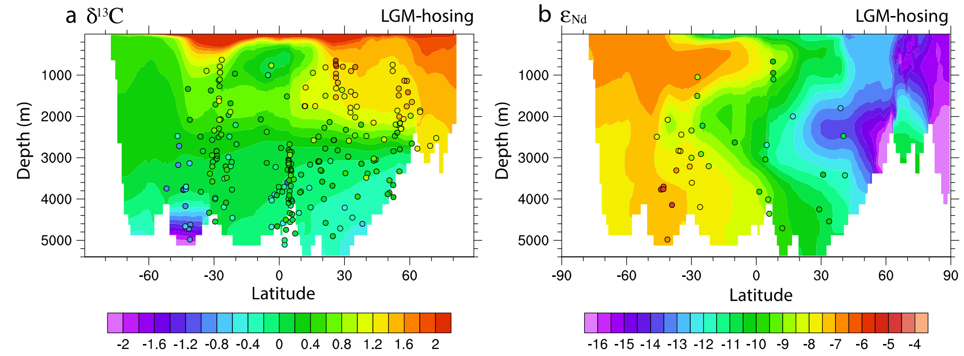

Fig. 7. Tracer distributions in LGM-hosing. (a) Atlantic zonal mean $\delta^{13}C$ with the LGM $\delta^{13}C$ reconstructions (Peterson et al., 2014) overlaid as colored circles. (b) Atlantic zonal mean ε_{Nd} with the LGM ε_{Nd} reconstructions (Howe et al., 2016) overlaid as colored circles.

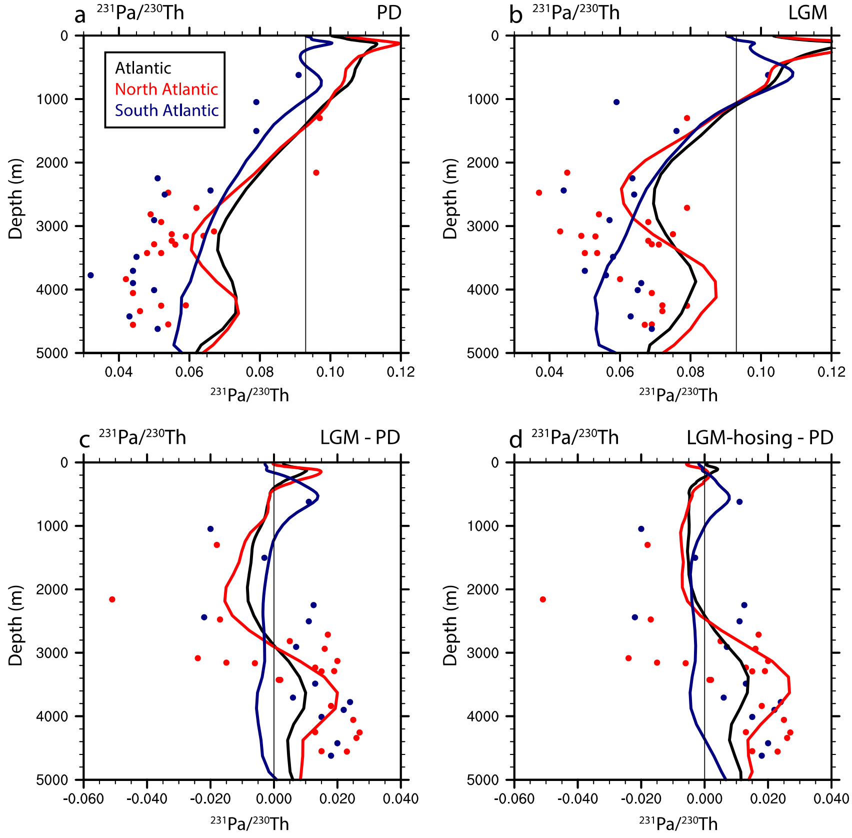

Fig. 8. Atlantic ^{231}Pa/^{230}Th profiles: Atlantic average (black); North Atlantic average (10°N-45°N) (red); South Atlantic average (10°S-34°S) (blue): (a) PD; (b) LGM; (c) difference between LGM and PD; (d) difference between LGM-hosing and PD. The ^{231}Pa/^{230}Th observations (references listed in Table S5) are plotted in dots, with observations from the North Atlantic in red and observations from the South Atlantic in blue.

the LGM reconstructions, the fit of modeled PD (strong and deep AMOC) $\delta^{13}C$ and ε_{Nd} with glacial observations is much worse than for either the LGM (strong and shallow AMOC) or the LGM-hosing (weak and shallow AMOC) simulations (Table S1). Therefore, the water mass tracers of $\delta^{13}C$ and ε_{Nd} provide essential information about the AMOC geometry, but not on AMOC strength (LeGrand and Wunsch, 1995). In other words, the simulation of the LGM $\delta^{13}C$ and ε_{Nd} distributions depends most critically on the shallower AMOC geometry instead of the AMOC strength.

4.2. ^{231}Pa/^{230}Th

Due to the large site-by-site model ^{231}Pa/^{230}Th deviation from observations caused by the model deficiency, likely including the particle flux effect, and observational uncertainties in individual sites, we compare the broad features of the ^{231}Pa/^{230}Th changes in the Atlantic between LGM and PD in model with reconstructions (SM text 4). The major feature of the observational LGM-PD difference is reduced LGM values from 1000 m to 3000 m and increased LGM values under 3000 m. This feature is captured by the model, although the magnitude of the change is smaller in the model than the observations, especially at the mid-depth (Fig. 8c). The lower LGM ^{231}Pa/^{230}Th than PD around 2000 m occurs mainly in the North Atlantic and is caused by the shallowing AMOC upper cell during the LGM; the higher LGM ^{231}Pa/^{230}Th below 3000 m in the North Atlantic is caused by the shoaling AMOC (Luo et al., 2010) and the increased strength of the AABW cell during the LGM. The enhanced AABW cell transports more ^{231}Pa than ^{230}Th northward from the South Atlantic to the North Atlantic, leading to the decrease in the South Atlantic and the increase in the North Atlantic (Fig. 8c).

$^{231}Pa/^{230}Th$ is much more sensitive to AMOC strength than $\delta^{13}C$ and ε_{Nd} are. At the level of outflowing branch of the AMOC upper cell (~2000 m), the model $^{231}Pa/^{230}Th$ in the North Atlantic decreases from the PD twice as large in the LGM than in LGM-hosing (−0.015 for LGM-PD and −0.006 for LGM-hosing - PD) (Fig. 8d and S4e and g), consistent with twice the strength of AMOC at LGM relative to LGM-hosing. If the model sensitivity of $^{231}Pa/^{230}Th$ to AMOC strength is correct and the average observational decrease of −0.03 represents the average value of the North Atlantic, the comparison between LGM and LGM-hosing suggests that the LGM AMOC upper cell strength was not weaker but was probably stronger than the PD. However, the model $^{231}Pa/^{230}Th$ deficiency and limited observational sites hinder a quantitative model-data comparison. There are six observational sites located between 1500 m and 2500 m, with the two North Atlantic sites showing an average decrease of −0.03, while four South Atlantic sites show a decrease in the eastern Atlantic and an increase in the western Atlantic (Figure S4e and f). While the North Atlantic sites may appear to be consistent with the model, the consistency is not clear in the South Atlantic. It is possible that the changes in the South Atlantic sites are influenced by the particle fluxes (SM text 4). In any case, these few data sites may not be sufficient to infer the basin average. Therefore, the current model $^{231}Pa/^{230}Th$ accuracy does not allow for a quantitative constraint of the AMOC strength from the available observations of $^{231}Pa/^{230}Th$. However, the sensitivity of $^{231}Pa/^{230}Th$ in our model suggests that, in the future, with increased observations in the mid-depth North Atlantic, and improved model simulation of $^{231}Pa/^{230}Th$, the LGM AMOC strength may be better constrained. This contrasts with $\delta^{13}C$ and ε_{Nd} discussed above, which are unlikely to provide an effective constrain on the LGM AMOC, even with increased observations and improved model simulations.

The $^{231}Pa/^{230}Th$ difference between the LGM and PD from a single site cannot constrain the LGM AMOC strength ambiguously. The $^{231}Pa/^{230}Th$ from the Bermuda Rise site (4550-m, 34°N, 58°W) suggests higher $^{231}Pa/^{230}Th$ during the LGM than the PD, which is interpreted as a 30-40% weaker LGM AMOC (McManus et al., 2004). Our model LGM $^{231}Pa/^{230}Th$ (0.078) from the Bermuda Rise is 0.016 higher than the PD (0.062), which agrees with the value of 0.013 in McManus et al. (2004). $^{231}Pa/^{230}Th$ in the abyssal North Atlantic is overall higher during LGM than PD but the model LGM AMOC is not weaker than PD. The relationship between AMOC and $^{231}Pa/^{230}Th$ from one site is complicated by AMOC strength, AMOC geometry, and for deep sites, by AABW cell strength as well (Luo et al., 2010). As a result, the higher glacial $^{231}Pa/^{230}Th$ from the Bermuda Rise is not simply related to AMOC strength but results from both the shallower of the AMOC upper cell and the stronger AABW transport. Therefore, with the different AMOC geometry and different AABW transport between LGM and PD, the interpretation of $^{231}Pa/^{230}Th$ in the Atlantic is not solely related to AMOC upper cell strength.

4.3. $\delta^{18}O_C$ gradient

The $\delta^{18}O_C$ gradient from the Florida Straits is smaller during the LGM than the PD, which suggests weaker Gulf Stream and therefore weaker AMOC during the LGM (Lynch-Stieglitz et al., 2014, 1999). It has been suggested that this weaker Gulf Stream was caused by the off-shore shift of the western boundary current (WBC) during the LGM, which is strengthened under glacial ice sheet topography (Gong et al., 2015). However, this explanation contradicts the finding based on planktonic $\delta^{18}O$ that the western boundary flow was primarily confined in the Florida Straits at LGM (LeGrande and Lynch-Stieglitz, 2007) and also the finding that lower glacial sea level has little impact on the geostrophic transport through the Florida Straits, as indicated by a regional ocean model (Ionita et al., 2009). In our simulation, because of the coarse resolution, the WBC is not well enough resolved to identify the off shore shift suggested by Gong et al. (2015). In our model, the $\delta^{18}O_C$ gradient is at 0.44 at LGM and 0.3 at PD, while observations suggest 0.4 at LGM and 0.6 at PD. Although the relative magnitude of the $\delta^{18}O_C$ gradient between LGM and PD does not agree with the observations, the model is self-consistent as the model $\delta^{18}O_C$ gradient also suggests a slightly stronger LGM AMOC in the model. Furthermore, the $\delta^{18}O_C$ gradient from the Florida Straits tracks the AMOC strength during the deglaciation (Gu et al., 2019b), suggesting that the $\delta^{18}O_C$ gradient from the Florida Straits may offer an unambiguous measure of AMOC intensity.

4.4. Physical mechanism for glacial AMOC strength

Regardless of the uncertainty on the AMOC strength, it is reasonable to suggest that the difference of AMOC intensity between LGM and PD is modest, relative to those during the extreme millennial events such as Heinrich event 1 and Younger Dryas, when more abundant evidence exists for a weaker AMOC intensity than the present (e.g., Lynch-Stieglitz et al., 2014; McManus et al., 2004). Given the dramatic climate change at LGM, it is natural to ask why the LGM AMOC change was relatively modest. Climate model simulations have shown a robust AMOC slowdown over the 20th century in response to the increased anthropogenic CO_2 and the resulted surface heat flux over the North Atlantic (Gregory et al., 2005) and this AMOC slowdown may be detected in observations (e.g., Rahmstorf et al., 2015). Given the large (~100ppm) decrease of CO_2 at LGM, one might then argue that the LGM AMOC should have been significantly stronger than PD. However, the deglacial CO_2 change occurred on millennial and longer time scales. Modeling studies suggest a robust AMOC weakening in response to the slow decrease of CO_2/enhancement of AMOC in response to the slow increase of CO_2, opposite to the expectation from the rapid anthropogenic warming case (e.g., Liu et al., 2005; Zhu et al., 2014a). This slow response of AMOC increase from the LGM to PD is caused by the reduction of Southern Ocean sea ice, brine injection, northward AABW export, followed by stratification change in the deep North Atlantic (Liu et al., 2005; Zhu et al., 2014a; Jansen, 2017). This quasi-equilibrium AMOC response is also accompanied by an opposite response to forcing by the large glacial continental ice sheets. The Laurentide Ice Sheet shifts the westerly jet southward during LGM, decreases wind stress, and sea ice expands over the subpolar North Atlantic, increasing the surface heat loss and then strengthening the AMOC (Zhu et al., 2014b; Gong et al., 2015), opposite to the weakening AMOC response to glacial CO_2 forcing. This compensation response to glacial CO_2 and ice sheet forcing can suppress the response of AMOC intensity, contributing to the conflicting results of glacial AMOC across models (Otto-Bliesner et al., 2007). In contrast, the robust shallowing of AMOC is determined mainly by the abyssal stratification, which is set by the Southern Ocean sea ice extent and brine injection through the AABW export. This in turn is determined predominantly by the atmospheric CO_2 (e.g., Jansen, 2017; Liu et al., 2005) and therefore should be more robust.

5. Conclusion

We have assessed the potential capability of multiple proxies in constraining the LGM AMOC and water mass distribution using the iPOP2 model simulations. In particular, we focused on addressing two questions.

1. Can the glacial Atlantic water mass distribution be constrained by water mass tracers?

Our model suggests a shallower than PD glacial NADW and AABW dominating over NADW in the deep Atlantic, which can be constrained accurately by modelled $\delta^{13}C_{AS}$. In comparison, water mass tracer ε_{Nd} may exhibit a bias in the deep North Atlantic, due to the source from continental margins and the reversible scavenging by particle fluxes, which can be further tested in other climate models and also water mass distribution reconstructed from other tracers in the future.

2. What tracers can be used to constrain the AMOC intensity?

Water mass tracers such as $\delta^{13}C$ and ε_{Nd} are not very sensitive to, and therefore may not provide a strong constraint on AMOC intensity. ^{231}Pa/^{230}Th is more sensitive to AMOC intensity and at times may provide a good constraint on AMOC strength. However, when the AMOC geometry and AABW transport change substantially, such as the case of LGM, ^{231}Pa/^{230}Th observations may reflect changes in water mass geometry and AABW transport more than the AMOC intensity, and therefore its capability in constraining AMOC intensity can be compromised. Future modelling studies, however, could identify the locations of ^{231}Pa/^{230}Th sites that can be used to constrain glacial AMOC intensity. In comparison, the $\delta^{18}O_c$ reconstruction of the upper ocean boundary current seems to provide a consistent measure of the AMOC intensity during the deglacial period, potentially providing a measure of AMOC intensity.

Finally, based on modeling studies available, we suggest that a moderate AMOC intensity difference between the LGM and PD, which is caused by the compensation of glacial CO_2 forcing and ice sheet forcing, while the shallowing of AMOC upper cell is controlled predominately by the CO_2 forcing over the Southern Ocean.

We caution that our model has some deficiencies, including both the physical model and isotope model, as well as its coarse resolution. Therefore, studies using independent models will be highly desirable for confirming our findings of the potential utility of multiple tracers in constraining the LGM AMOC and water mass distribution. Increased proxy observation and more advanced data assimilation schemes can be used to reconstruct the AMOC with higher fidelity.

Declaration of competing interest

The authors declare that they have no known competing financial interests or personal relationships that could have appeared to influence the work reported in this paper.

Acknowledgements

We thank two anonymous reviewers for their useful and constructive comments. We also thank Editor Dr Laura F. Robinson for handling the manuscript. This work is supported by National Science Foundation of China No. 41630527, US National Science Foundation (NSF) P2C2 projects (1401778, 1401802, and 1566432). We would like to acknowledge the high-performance computing support from Yellowstone (ark:/85065/d7wd3xhc) and Cheyenne (doi:10.5065/D6RX99HX) provided by NCAR's Computational and Information Systems Laboratory, sponsored by the National Science Foundation and from Center for High Performance Computing and System Simulation, Pilot National Laboratory for Marine Science and Technology (Qingdao). Data used to produce the results in this study can be obtained from HPSS at CISL: /home/sgu28/CTRACE_decadal or by contacting the authors.

Appendix A. Supplementary material

Supplementary material related to this article can be found online at https://doi.org/10.1016/j.epsl.2020.116294.

References

Böhm, E., Lippold, J., Gutjahr, M., Frank, M., Blaser, P., Antz, B., Fohlmeister, J., Frank, N., Andersen, M.B., Deininger, M., 2014. Strong and deep Atlantic meridional overturning circulation during the last glacial cycle. Nature. https://doi.org/10.1038/nature14059.

Broecker, W.S., Maier-Reimer, E., 1992. The influence of air and sea exchange on the carbon isotope distribution in the sea. Glob. Biogeochem. Cycles 6, 315–320.

Curry, W.B., Oppo, D.W., 2005. Glacial water mass geometry and the distribution of δ13 C of ΣCO2 in the western Atlantic Ocean. Paleoceanography 20. https://doi.org/10.1029/2004PA001021.

Danabasoglu, G., Bates, S.C., Briegleb, B.P., Jayne, S.R., Jochum, M., Large, W.G., Peacock, S., Yeager, S.G., 2012. The CCSM4 ocean component. J. Climate 25, 1361–1389. https://doi.org/10.1175/JCLI-D-11-00091.1.

Freeman, E., Skinner, L.C., Waelbroeck, C., Hodell, D., 2016. Radiocarbon evidence for enhanced respired carbon storage in the Atlantic at the Last Glacial Maximum. Nat. Commun. 7, 1–8. https://doi.org/10.1038/ncomms11998.

Gebbie, G., 2014. How much did glacial North Atlantic water shoal? Paleoceanography 29, 190–209. https://doi.org/10.1002/2013PA002557.

Gong, X., Zhang, Xiangdong, Lohmann, G., 2015. Higher Laurentide and Greenland ice sheets strengthen the North Atlantic ocean circulation. Clim. Dyn. 45, 139–150. https://doi.org/10.1007/s00382-015-2502-8.

Gregory, J.M., Dixon, K.W., Stouffer, R.J., Weaver, A.J., Driesschaert, E., Eby, M., Fichefet, T., Hasumi, H., Hu, A., Jungclaus, J.H., Kamenkovich, I.V., Levermann, A., Montoya, M., Murakami, S., Nawrath, S., Oka, A., Sokolov, A.P., Thorpe, R.B., 2005. A model intercomparison of changes in the Atlantic thermohaline circulation in response to increasing atmospheric CO2 concentration. Geophys. Res. Lett. 32, 1–5. https://doi.org/10.1029/2005GL023209.

Gu, S., Liu, Z., 2017. 231Pa and 230Th in the ocean model of the community Earth system model (CESM1.3). Geosci. Model Dev. 10, 4723–4742. https://doi.org/10.5194/gmd-10-4723-2017.

Gu, S., Liu, Z., Zhang, J., Rempfer, J., Joos, F., Oppo, D.W., 2017. Coherent response of Antarctic intermediate water and Atlantic meridional overturning circulation during the last deglaciation: reconciling contrasting neodymium isotope reconstructions from the tropical Atlantic. Paleoceanography 32, 1036–1053. https://doi.org/10.1002/2017PA003092.

Gu, S., Liu, Z., Jahn, A., Rempfer, J., Zhang, J., Joos, F., 2019a. Modeling neodymium isotopes in the ocean component of the CESM1. J. Adv. Model. Earth Syst., 624–640. https://doi.org/10.1029/2018MS001538.

Gu, S., Liu, Z., Lynch-Stieglitz, J., Jahn, A., Zhang, J., Lindsay, K., Wu, L., 2019b. Assessing the ability of zonal d18O contrast in benthic foraminifera to reconstruct deglacial evolution of Atlantic meridional overturning circulation. Paleoceanogr. Paleoclimatol. 34. https://doi.org/10.1029/2019PA003564.

Hesse, T., Butzin, M., Bickert, T., Lohmann, G., 2011. A model-data comparison of δ^{13}C in the glacial Atlantic Ocean. Paleoceanography 26, 1–16. https://doi.org/10.1029/2010PA002085.

Howe, J.N.W., Piotrowski, A.M., Noble, T.L., Mulitza, S., Chiessi, C.M., Bayon, G., 2016. North Atlantic Deep Water Production during the Last Glacial Maximum. Nat. Commun. 7, 11765. https://doi.org/10.1038/ncomms11765.

Ionita, D.A., Di Lorenzo, E., Lynch-Stieglitz, J., 2009. Effect of lower sea level on geostrophic transport through the Florida Straits during the Last Glacial Maximum. Paleoceanography 24, 1–7. https://doi.org/10.1029/2009PA001820.

Jahn, A., Lindsay, K., Giraud, X., Gruber, N., Otto-Bliesner, B.L., Liu, Z., Brady, E.C., 2015. Carbon isotopes in the ocean model of the Community Earth System Model (CESM1). Geosci. Model Dev. 8, 2419–2434. https://doi.org/10.5194/gmd-8-2419-2015.

Jansen, M.F., 2017. Glacial ocean circulation and stratification explained by reduced atmospheric temperature. Proc. Natl. Acad. Sci. 114, 45–50. https://doi.org/10.1073/pnas.1610438113.

Kurahashi-Nakamura, T., Paul, A., Losch, M., 2017. Dynamical reconstruction of the global ocean state during the Last Glacial Maximum. Paleoceanography 32, 326–350. https://doi.org/10.1002/2016PA003001.

Large, W.G., Yeager, S.G., 2008. The global climatology of an interannually varying air–sea flux data set. Clim. Dyn. 33, 341–364. https://doi.org/10.1007/s00382-008-0441-3.

LeGrand, P., Wunsch, C., 1995. Constraints from palaeo-tracer data on the North Atlantic circulation during the Last Glacial Maximum. Paleoceanography 10, 1011–1045.

LeGrande, A.N., Lynch-Stieglitz, J., 2007. Surface currents in the western North Atlantic during the Last Glacial Maximum. Geochem. Geophys. Geosyst. 8. https://doi.org/10.1029/2006GC001371.

Lippold, J., Luo, Y., Francois, R., Allen, S.E., Gherardi, J., Pichat, S., Hickey, B., Schulz, H., 2012. Strength and geometry of the glacial Atlantic meridional overturning circulation. Nat. Geosci. 5, 813–816. https://doi.org/10.1038/ngeo1608.

Liu, Z., Shin, S.-I., Webb, R.S., Lewis, W., Otto-Bliesner, B.L., 2005. Atmospheric CO2 forcing on glacial thermohaline circulation and climate. Geophys. Res. Lett. 32, L02706. https://doi.org/10.1029/2004GL021929.

Liu, Z., Otto-Bliesner, B.L., He, F., Brady, E.C., Tomas, R., Clark, P.U., Carlson, a E., Lynch-Stieglitz, J., Curry, W., Brook, E., Erickson, D., Jacob, R., Kutzbach, J., Cheng, J., 2009. Transient simulation of last deglaciation with a new mechanism for

Bolling-Allerod warming. Science 325, 310–314. https://doi.org/10.1126/science.1171041.

Luo, Y., Francois, R., Allen, S., 2010. Sediment 231Pa/230Th as a recorder of the rate of the Atlantic meridional overturning circulation: insights from a 2-D model. Ocean Sci. 6, 381–400. https://doi.org/10.5194/os-6-381-2010.

Lynch-Stieglitz, J., Fairbanks, R.G., 1994. A conservative tracer for glacial ocean circulation from carbon-isotope and palaeo-nutrient measurements in benthic foraminifera. Nature 369, 308–310.

Lynch-Stieglitz, J., Curry, W.B., Slowey, N., 1999. Weaker Gulf Stream in the Florida straits during the Last Glacial Maximum. Nature 402, 644–648. https://doi.org/10.1038/45204.

Lynch-Stieglitz, J., Schmidt, M.W., Henry, G.L., Curry, W.B., Skinner, L.C., Mulitza, S., Zhang, R., Chang, P., 2014. Muted change in Atlantic overturning circulation over some glacial-aged Heinrich events. Nat. Geosci. 7, 144–150. https://doi.org/10.1038/ngeo2045.

Mahowald, N.M., Muhs, D.R., Levis, S., Rasch, P.J., Yoshioka, M., Zender, C.S., Luo, C., 2006. Change in atmospheric mineral aerosols in response to climate: last glacial period, preindustrial, modern, and doubled carbon dioxide climates. J. Geophys. Res., Atmos. 111. https://doi.org/10.1029/2005JD006653.

Marchitto, T.M., Broecker, W.S., 2006. Deep water mass geometry in the glacial Atlantic Ocean: a review of constraints from the paleonutrient proxy Cd/Ca. Geochem. Geophys. Geosyst. 7. https://doi.org/10.1029/2006GC001323.

Marzocchi, A., Jansen, M.F., 2017. Connecting Antarctic sea ice to deep-ocean circulation in modern and glacial climate simulations. Geophys. Res. Lett. 44, 6286–6295. https://doi.org/10.1002/2017GL073936.

McManus, J., Francois, R., Gherardi, J., 2004. Collapse and rapid resumption of Atlantic meridional circulation linked to deglacial climate changes. Nature 428, 834–837.

Menviel, L., Yu, J., Joos, F., Mouchet, A., Meissner, K.J., England, M.H., 2017. Poorly ventilated deep ocean at the Last Glacial Maximum inferred from carbon isotopes: a data-model comparison study. Paleoceanography 32, 2–17. https://doi.org/10.1002/2016PA003024.

Middag, R., van Heuven, S.M.A.C., Bruland, K.W., de Baar, H.J.W., 2018. The relationship between cadmium and phosphate in the Atlantic Ocean unravelled. Earth Planet. Sci. Lett. 492, 79–88. https://doi.org/10.1016/j.epsl.2018.03.046.

Muglia, J., Schmittner, A., 2015. Glacial Atlantic overturning increased by wind stress in climate models. Geophys. Res. Lett. 42, 9862–9869. https://doi.org/10.1002/2015GL064583.

Muglia, J., Skinner, L.C., Schmittner, A., 2018. Weak overturning circulation and high Southern Ocean nutrient utilization maximized glacial ocean carbon. Earth Planet. Sci. Lett. 496, 47–56. https://doi.org/10.1016/j.epsl.2018.05.038.

Ng, H.C., Robinson, L.F., McManus, J.F., Mohamed, K.J., Jacobel, A.W., Ivanovic, R.F., Gregoire, L.J., Chen, T., 2018. Coherent deglacial changes in western Atlantic Ocean circulation. Nat. Commun. 9, 1–10. https://doi.org/10.1038/s41467-018-05312-3.

Oppo, D.W., Gebbie, G., Huang, K.-F., Curry, W.B., Marchitto, T.M., Pietro, K.R., 2018. Data constraints on glacial Atlantic water mass geometry and properties. Paleoceanogr. Paleoclimatol. 33 (9), 1013–1034. https://doi.org/10.1029/2018PA003408.

Otto-Bliesner, B.L., Hewitt, C.D., Marchitto, T.M., Brady, E., Abe-Ouchi, A., Crucifix, M., Murakami, S., Weber, S.L., 2007. Last Glacial Maximum ocean thermohaline circulation: PMIP2 model intercomparisons and data constraints. Geophys. Res. Lett. 34, 1–6. https://doi.org/10.1029/2007GL029475.

Peterson, C.D., Lisiecki, L.E., Stern, J.V., 2014. Deglacial whole-ocean δ13C change estimated from 480 benthic foraminiferal records. Paleoceanography 29 (6), 549–563. https://doi.org/10.1002/2013PA002552.

Rahmstorf, S., Box, J.E., Feulner, G., Mann, M.E., Robinson, A., Rutherford, S., Schaffernicht, E.J., 2015. Exceptional twentieth-century slowdown in Atlantic Ocean overturning circulation. Nat. Clim. Change 5, 475–480. https://doi.org/10.1038/nclimate2554.

Rempfer, J., Stocker, T.F., Joos, F., Dutay, J.-C., Siddall, M., 2011. Modelling Nd-isotopes with a coarse resolution ocean circulation model: sensitivities to model parameters and source/sink distributions. Geochim. Cosmochim. Acta 75, 5927–5950. https://doi.org/10.1016/j.gca.2011.07.044.

Schmittner, A., Lund, D.C., 2015. Early deglacial Atlantic overturning decline and its role in atmospheric CO2 rise inferred from carbon isotopes (δ13C). Clim. Past 11, 135–152. https://doi.org/10.5194/cp-11-135-2015.

Weber, S.L., Drijfhout, S.S., Abe-Ouchi, A., Crucifix, M., Eby, M., Ganopolski, A., Murakami, S., Otto-Bliesner, B., Peltier, W.R., 2007. The modern and glacial overturning circulation in the Atlantic Ocean in PMIP coupled model simulations. Clim. Past 3, 51–64. https://doi.org/10.5194/cpd-2-923-2006.

Yu, E.-F., Francois, R., Bacon, M.P., 1996. Similar rates of modern and last-glacial ocean thermohaline circulation inferred from radiochemical data. Nature. https://doi.org/10.1038/379689a0.

Zhang, J., 2016. Understanding the deglacial evolution of deep Atlantic water masses in an isotope-enabled ocean model. Ph.D. thesis. Atmospheric and Oceanic Sciences, University of Wisconsin Madison.

Zhang, J., Liu, Z., Brady, E.C., Jahn, A., Oppo, D.W., Clark, P.U., Marcott, S.A., Lindsay, K., 2017. Asynchronous warming and oxygen isotope evolution of deep Atlantic water masses during the last deglaciation. Proc. Natl. Acad. Sci. 114, 11075–11080. https://doi.org/10.1073/pnas.1704512114.

Zhang, X., Lohmann, G., Knorr, G., Xu, X., 2013. Different ocean states and transient characteristics in Last Glacial Maximum simulations and implications for deglaciation. Clim. Past 9, 2319–2333. https://doi.org/10.5194/cp-9-2319-2013.

Zhu, J., Liu, Z., Zhang, J., Liu, W., 2014a. AMOC response to global warming: dependence on the background climate and response timescale. Clim. Dyn. 44, 3449–3468. https://doi.org/10.1007/s00382-014-2165-x.

Zhu, J., Liu, Z., Zhang, X., Eisenman, I., Liu, W., 2014b. Linear weakening of the AMOC in response to receding glacial ice sheets in CCSM3. Geophys. Res. Lett., 6252–6258. https://doi.org/10.1002/2014GL060891.Received.